Shape Sensing with Sparse Strain Information for Aerospace Applications

Paolo Minigher[1,2*], Janto Gundlach[2*], Saullo G. P. Castro[1*], Yves Govers[2]

[1] *Department of Structures and Materials, Faculty of Aerospace Engineering, Delft University of Technology, Kluyverweg 1, 2629HS Delft, The Netherlands*

[2] *Institute of Aeroelasticity, Department of Structural Dynamics and System Identification, German Aerospace Center (DLR), Bunsenstraße 10, 37073 Göttingen, Germany*

Abstract

The reconstruction of the deformations from strain measurements is usually called *shape sensing* and is of interest in the field of structural health monitoring. In this paper the problem is studied with a limited amount of strain data since for real applications and an on-line monitoring it might be unfeasible to employ a large amount of sensors. In this context the deformations are computed with the inverse Finite Element Method (iFEM) taking advantage from a preliminary strain pre-extrapolation done with the Smoothing Element Analysis (SEA). The results are then compared with another common shape sensing method, the so-called Modal Method (MM), using as study case a composite wing-like structure. Noise and uncertainties and their influences on the results are also assessed. The outcome obtained points out that iFEM is largely improved after the preliminary strain pre-extrapolation. However, for this study case, the Modal Method performs better despite the intrinsic disadvantage in requiring the material properties of the structure (compared to iFEM, where no constitutive relation is needed), which affects the results in case uncertainties are present in the system.

Keywords: Structural Health Monitoring, Shape Sensing, iFEM, Modal Method, Uncertainty Quantification

1. Introduction

Structural life management has become an increasingly important factor in aerospace, the wind energy sector and basically all fields involving high-performing structures. Such management involves on-line monitoring that is able to constantly measure how the structure is deforming over the span of its lifetime, thus enabling lightweight designs that are more aggressive in terms of exploiting the material strength and damage tolerance. A real-time reconstruction of the deformed structural shape using in-situ strain measurements would allow one to indirectly access the full strain and stress fields, failure states and in general to improve the Structural Health Monitoring of the structure. Some methods that give the capability to compute the displacements directly from the strain measurements have emerged. In particular, the so-called inverse Finite Element Method (iFEM) [1] and the Modal Method (MM) [2] are often used and proved to be among the most reliable and accurate methods developed in literature. Several studies and comparisons were carried out in previous works, such as in Esposito et al. (2020) [3] where the main existing approaches are compared, with the authors highlighting the accuracy of iFEM and MM. Usually, a large number of sensors is employed in these studies, which is not crucial for numerical applications since the strain values come directly from the FE model. However, in real applications the strain information is highly limited due to: the difficulty in installing strain sensors; the weight and complexity of the cables and the data acquisition system; the difficulty in accessing many regions of the structure, and the overall costs attributed to the measurements.

Therefore, the primary aim of the present study is to recover the structural deformations in the case where the strain measurements are limited and the sensors are sparsely distributed over the structural domain. It is known that the standard iFEM can lead to poor results with the use of sparse strain data [4], and therefore the present study proposes the use of a pre-extrapolation of the strain field as suggested by Oboe et al. (2021) [4]. That is, from a sparse discrete set of strain measurements, the strain field is estimated over the whole structural domain and this is used as an input for iFEM. Since the study case herein presented is characterized by a rather complex geometry, the strain pre-extrapolation is done with the so-called Smoothing Element Analysis (SEA) [5], by employing a novel four-node element.

The study is structured as follows. Section 2 presents the study case with the focus on wing-like structures. Section 3 briefly outlines the necessary background knowledge and describes the main features of the Modal Method, iFEM and SEA. Section 4 points out some difficulties coming from SEA using the available three-node element from literature [6] and the introduction of a novel four-node SEA element which showed to be less sensitive to the choice of some scalar parameters. In Section 5, iFEM is coupled with SEA in order to obtain a better estimation of the displacement field. Then, a comparison with the Modal Method is carried out in Section 6, and later in Section 7 the

---

⋆Corresponding authors: paolo.minigher.98@gmail.com, Janto.Gundlach@dlr.de, S.G.P.Castro@tudelft.nl

measurement and system uncertainties are taken into account. Finally, the conclusions are presented in Section 8.

2. Study case and virtual sensor positions

A simplified model of a skin-carrying load wing is taken into consideration, consisting of a simple GFRP shell filled with layers of foam that has been manufactured (Figure 1a) to represent a demonstrator of the ISTAR research aircraft[1].

(a) *ISTAR demonstrator.*
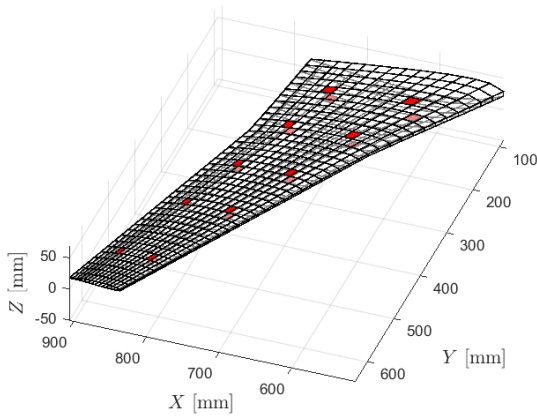
(b) *Sensor positions (red elements) on the mesh of the wing.*

Figure 1: *Study case: real model and FE model used for to extract the experimental strain measurements.*

All the strain information is taken from the corresponding FE model [7] which is an altered version of [8]. In particular, 20 virtual strain rosettes are considered to be installed on the wing skin, all aligned with the material reference system that is parallel to the leading edge of the outer section of the wing. The spatial distribution of the sensors is sparse and homogeneous, as illustrated in Figure 1b and is specified in [7]. The strains have been extracted from the centroids of the elements highlighted. The material properties used are the ones from Table 1,

while Table 2 reports the layup specifications, where for fabrics the corresponding thickness of each ply is halved.

On the structure, three different load cases are applied (Figure 3): a tip concentrated force and two pressure fields on the bottom skin (respectively, a constant and a parabolic one). Given that the performances of the methods depend in general on the strain field developed by the structure and on its complexity, in this way the results obtained are assessed for three different loading conditions with the aim to see if the conclusions which can be drawn are sufficiently general.

As a final note, it is important to point out that in this study only virtual strain rosettes are used. So for the pseudo-instrumented inverse elements (later used for iFEM), every in-plane strain component is defined and the strain field can be rotated in the element reference system without any problem. If this was not the case, then it would still be possible to define the strain in the element local reference system thanks to the strain pre-extrapolation described in the following. However, this would mix experimental strain measurements with estimated ones, influencing the weights given to the inverse elements.
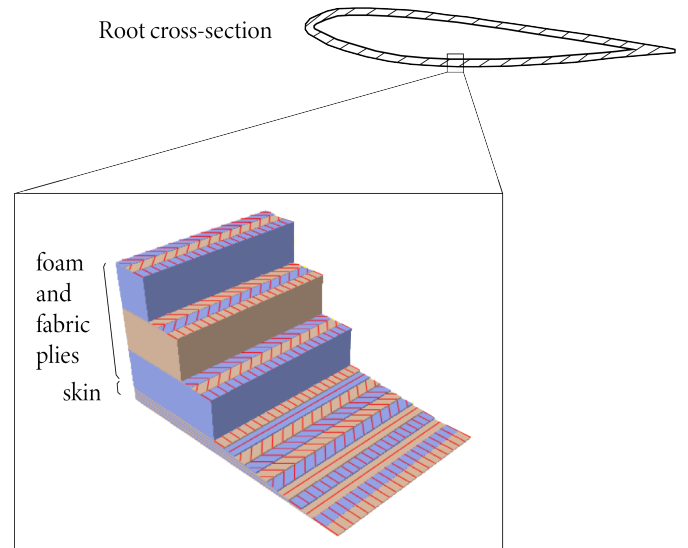

Figure 2: *Layup of demonstrator skin.*

	E_1	E_2	ν_{12}	G_{12}
fiber-glass ply	41.75 GPa	12.94 GPa	0.26	4.96 GPa
foam	0.092 GPa	–	0.4	–
	G_{13}	G_{23}		
fiber-glass ply	4.13 GPa	4.13 GPa		
foam	–	–		

Table 1: *Material properties of fiber-glass plies.*

---

[1]Dassault Falcon 2000LX DLR research aircraft.

#ply	Thickness	Orientation
1 (paint)	$3.5e-5$ m	$0°$
2, 3	$8.525e-6$ m	$0°/90°$
4, 5	$5.456e-5$ m	$0°/90°$
6, 7	$5.456e-5$ m	$-45°/45°$
8, 9	$5.456e-5$ m	$45°/-45°$
10, 11	$5.456e-5$ m	$90°/0°$
12 (foam)	0.0015 m	$0°$
13, 14	$1.67e-5$ m	$-45°/45°$
15 (foam)	0.0015 m	$0°$
16, 17	$1.67e-5$ m	$-45°/45°$
18 (foam)	0.0015 m	$0°$
19, 20	$1.67e-5$ m	$-45°/45°$

Table 2: *Thickness and orientation of plies.*

(a) *Tip load:* $P = 10^2$ N.

(b) *Constant pressure:*
$p(x,y) = 10^4$ Pa.

(c) *Parabolic pressure:*
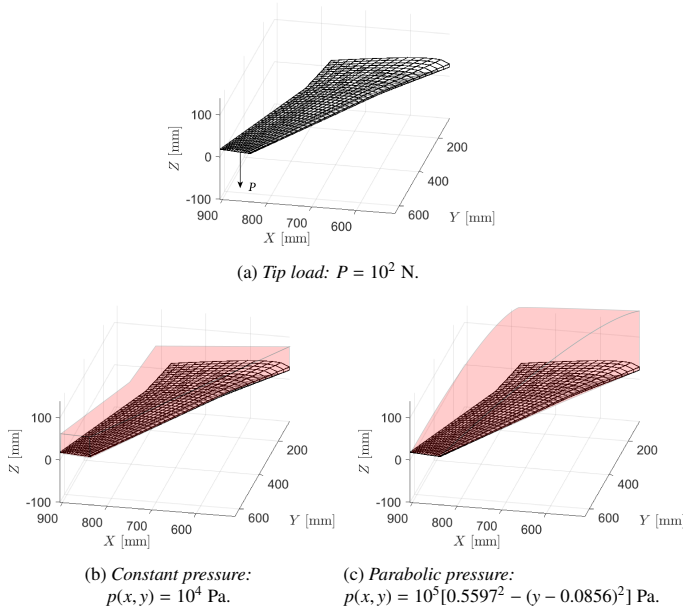$p(x,y) = 10^5[0.5597^2 - (y - 0.0856)^2]$ Pa.

Figure 3: *Load cases applied on the ISTAR demonstrator wing.*

3. Theoretical background

In this section the main features of the methods employed are explained. In particular a brief description of the Modal Method, iFEM and SEA are reported. The references quoted can be referred for more details.

3.1. Modal Method

The modal coordinates r can be related to the actual degrees of freedom of the system u as:

$$u = \Phi r \tag{1}$$

where Φ is the mode shape matrix. Analogously, for the strains a similar relation holds:

$$\varepsilon^\varepsilon = \Psi r \tag{2}$$

where Ψ is the so-called matrix of strain modes which contains the strains for each corresponding deformation mode. Since from experimental measurements the strain values can be obtained, it is necessary to relate ε^ε (vector containing the experimental strains) with u. At first sight, this might be done simply noting that $r = \Psi^{-1}\varepsilon$, and therefore:

$$\underbrace{u}_{N\times1} = \underbrace{\Phi}_{N\times p} \underbrace{\Psi^{-1}}_{p\times m} \underbrace{\varepsilon^\varepsilon}_{m\times1} \tag{3}$$

where the dimension of each component is highlighted: N is the number of degrees of freedom of the system, p the number of mode shapes considered, and m the number of strain measures taken. In order to compute u it is required that the matrices used are square, or in other words that the number of strain measures m equals the number of modes used p. However, this is not always the case. Therefore, Eq.(2) can be solved using the pseudo-inverse matrix [2]:

$$r = (\Psi^T\Psi)^{-1}\Psi^T\varepsilon^\varepsilon \tag{4}$$

substituting in Eq.(1) it is possible to obtain:

$$u = \underbrace{\Phi(\Psi^T\Psi)^{-1}\Psi^T}_{\text{DST}}\varepsilon^\varepsilon \tag{5}$$

giving the value of all the degrees of freedom in which the structure is discretized. The matrix which relates u with r is commonly referred to as **DST**, the displacement-strain transformation matrix.

Several applications have been studied with this method (see for example [9, 10, 11]), bringing in general satisfactory results. The main drawback consists in the fact that the mode shapes have to be known in advance. Since these are generally computed with FEM, the material and geometrical properties of the structure have to be precisely known. Alternatively, experimental mode shapes could also be used.

3.2. inverse Finite Element Method

From the First Order Shear Deformation theory the following relations for the kinematic variables hold:

$$\begin{cases} u_x(x,y) = u + z\theta_y \\ u_y(x,y) = v - z\theta_x \\ u_z(x,y) = w \end{cases} \tag{6}$$

where u and v are the mid-plane displacements, θ_x and θ_y the positive rotations about the x and y axes and w the out-of-plane displacement (constant across the thickness). The in-

3

plane strains can be computed as:

$$\varepsilon_x = \frac{\partial u_x}{\partial x} = \underbrace{\frac{\partial u}{\partial x}}_{\varepsilon_{x0}} + z \underbrace{\frac{\partial \theta_y}{\partial x}}_{\kappa_{x0}}$$

$$\varepsilon_y = \frac{\partial u_y}{\partial y} = \underbrace{\frac{\partial v}{\partial y}}_{\varepsilon_{y0}} - z \underbrace{\frac{\partial \theta_x}{\partial y}}_{\kappa_{y0}} \qquad (7)$$

$$\gamma_{xy} = \frac{\partial u_x}{\partial y} + \frac{\partial u_y}{\partial x} = \underbrace{\frac{\partial u}{\partial y} + \frac{\partial v}{\partial x}}_{\gamma_{xy0}} + z \underbrace{\left(\frac{\partial \theta_x}{\partial x} - \frac{\partial \theta_y}{\partial y} \right)}_{\kappa_{xy0}}$$

which can be written as:

$$\begin{bmatrix} \varepsilon_x \\ \varepsilon_y \\ \gamma_{xy} \end{bmatrix} = \begin{bmatrix} \varepsilon_{x0} \\ \varepsilon_{y0} \\ \gamma_{xy0} \end{bmatrix} + z \begin{bmatrix} \kappa_{x0} \\ \kappa_{y0} \\ \kappa_{xy0} \end{bmatrix} \qquad (8)$$

$$= \boldsymbol{e}(\boldsymbol{u}) + z\boldsymbol{k}(\boldsymbol{u})$$

where $\boldsymbol{e}$ represents the membrane strain measures, $\boldsymbol{k}$ the curvatures and $\boldsymbol{u} = [u \ v \ w \ \theta_x \ \theta_y]^\top$ the kinematic variables. Similarly, also the transverse shear strain can be expressed as:

$$\boldsymbol{g}(\boldsymbol{u}) = \begin{bmatrix} \gamma_{xz} \\ \gamma_{yz} \end{bmatrix} = \begin{bmatrix} \dfrac{\partial w}{\partial x} + \theta_y \\ \dfrac{\partial w}{\partial y} - \theta_x \end{bmatrix} \qquad (9)$$

It is possible to obtain experimentally the values of the strain measures $\boldsymbol{e}$ and $\boldsymbol{k}$. Imagine that on both sides of a plate a strain rosette is installed as shown in Figure 4.
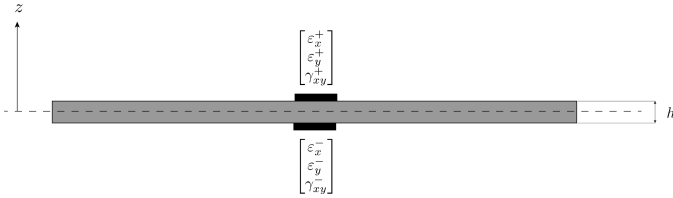

Figure 4: *Strain rosettes installed on both sides of a plate in order to measure membrane strains and curvatures.*

Then, taking for example just the ε_x strain measurement, it is possible to write:

$$\begin{cases} \varepsilon_x^+ = \varepsilon_{x0} + \dfrac{h}{2}\kappa_{x0} \\[2mm] \varepsilon_x^- = \varepsilon_{x0} - \dfrac{h}{2}\kappa_{x0} \end{cases} \qquad (10)$$

where $\bullet^+$ stands for example for the measurement on the top of the plate and $\bullet^-$ for the one on the bottom. Summing the two equations the membrane strain measurement can be easily computed:

$$\varepsilon_{x0} = \frac{1}{2} \left(\varepsilon_x^+ + \varepsilon_x^- \right) \qquad (11)$$

Subtracting the two equations:

$$\kappa_{x0} = \frac{1}{h} \left(\varepsilon_x^+ - \varepsilon_x^- \right) \qquad (12)$$

Repeating the procedure for the other components it is possible to finally obtain the experimental values for the membrane strain measures and curvature:

$$\boldsymbol{e}^\varepsilon = \begin{bmatrix} \varepsilon_{x0}^\varepsilon \\ \varepsilon_{y0}^\varepsilon \\ \gamma_{xy0}^\varepsilon \end{bmatrix} = \frac{1}{2} \left(\begin{bmatrix} \varepsilon_{xx}^+ \\ \varepsilon_{yy}^+ \\ \gamma_{xy}^+ \end{bmatrix} + \begin{bmatrix} \varepsilon_{xx}^- \\ \varepsilon_{yy}^- \\ \gamma_{xy}^- \end{bmatrix} \right)$$

$$\boldsymbol{k}^\varepsilon = \begin{bmatrix} \kappa_{x0}^\varepsilon \\ \kappa_{y0}^\varepsilon \\ \kappa_{xy0}^\varepsilon \end{bmatrix} = \frac{1}{h} \left(\begin{bmatrix} \varepsilon_{xx}^+ \\ \varepsilon_{yy}^+ \\ \gamma_{xy}^+ \end{bmatrix} - \begin{bmatrix} \varepsilon_{xx}^- \\ \varepsilon_{yy}^- \\ \gamma_{xy}^- \end{bmatrix} \right) \qquad (13)$$

The iFEM consists of minimizing a functional $\Phi^{(e)}$ representing the error between the experimental strain measures and the ones from the model; usually expressed as:

$$\Phi^{(e)}(\boldsymbol{u}^{(e)}) = w_e \|\boldsymbol{e}(\boldsymbol{u}^{(e)}) - \boldsymbol{e}^\varepsilon\|^2 + w_k \|\boldsymbol{k}(\boldsymbol{u}^{(e)}) - \boldsymbol{k}^\varepsilon\|^2 + w_g \|\boldsymbol{g}(\boldsymbol{u}^{(e)}) - \boldsymbol{g}^\varepsilon\|^2 \qquad (14)$$

where $\boldsymbol{u}^{(e)}$ are the element degrees of freedom, w_e, w_k and w_g are scalar weights whose role is described below and the norms are expressed as:

$$\left\| \boldsymbol{e}(\boldsymbol{u}^{(e)}) - \boldsymbol{e}^\varepsilon \right\|^2 = \frac{1}{n^{(e)}} \iint_{A^{(e)}} \sum_{i=1}^{n^{(e)}} \left[\boldsymbol{e}(\boldsymbol{u}^{(e)})_i - \boldsymbol{e}_i^\varepsilon \right]^2 dxdy$$

$$\left\| \boldsymbol{k}(\boldsymbol{u}^{(e)}) - \boldsymbol{k}^\varepsilon \right\|^2 = \frac{h^2}{n^{(e)}} \iint_{A^{(e)}} \sum_{i=1}^{n^{(e)}} \left[\boldsymbol{k}(\boldsymbol{u}^{(e)})_i - \boldsymbol{k}_i^\varepsilon \right]^2 dxdy \quad (15)$$

$$\left\| \boldsymbol{g}(\boldsymbol{u}^{(e)}) - \boldsymbol{g}^\varepsilon \right\|^2 = \frac{1}{n^{(e)}} \iint_{A^{(e)}} \sum_{i=1}^{n^{(e)}} \left[\boldsymbol{g}(\boldsymbol{u}^{(e)})_i - \boldsymbol{g}_i^\varepsilon \right]^2 dxdy$$

where $n^{(e)}$ is the number of strain measurements performed on the element (e) domain. Note that the norm related to $\boldsymbol{k}$ is multiplied by the thickness h for dimensional consistency. Before proceeding, note that it is not always possible to obtain experimental measures for every inverse element. This is already clear with regard to the transverse shear strain measurement $\boldsymbol{g}^\varepsilon$ which cannot be directly recovered. In these cases there is the need to maintain the connectivity between the elements, which can be done by modifying the definition of the error functional and acting on the weights w_e, w_k and w_g. When no strain measurement is present on an element, so that $\boldsymbol{e}^\varepsilon$ or $\boldsymbol{k}^\varepsilon$ or $\boldsymbol{g}^\varepsilon$ is missing, the norm definition becomes:

$$\left\| \boldsymbol{e}(\boldsymbol{u}^{(e)}) \right\|^2 = \iint_{A^{(e)}} \boldsymbol{e}(\boldsymbol{u}^{(e)})^2 dxdy$$

$$\left\| \boldsymbol{k}(\boldsymbol{u}^{(e)}) \right\|^2 = h^2 \iint_{A^{(e)}} \boldsymbol{k}(\boldsymbol{u}^{(e)})^2 dxdy \qquad (16)$$

$$\left\| \boldsymbol{g}(\boldsymbol{u}^{(e)}) \right\|^2 = \iint_{A^{(e)}} \boldsymbol{g}(\boldsymbol{u}^{(e)})^2 dxdy$$

and the corresponding weights assume relatively small values ($\approx 10^{-4}$ from literature [12, 13, 3, 14, 15]). Intuitively this

means that the minimization procedure in iFEM is hardly affected by these components, such that only the errors caused by measurement values are minimized. The approach of assuming small weight values for quantities that cannot be measured makes it possible to not only neglect the transverse shear component, but also to define so-called *strainless* elements where no strain measurement is done, allowing to estimate the displacement field also in regions formed by not-instrumented elements.

In order to discretize any complex geometry, it is convenient to interpolate the continuum displacement field by means of suitable finite elements. A four-node inverse element named iQS4 was developed by Kefal et al. (2016) [12], built with a drilling rotation degree of freedom, containing 6 degrees of freedom per node, being 3 translations and 3 rotations. The interpolation of the kinematic variables is given by:

$$
\begin{aligned}
u(x, y) &= \boldsymbol{N}\boldsymbol{u} + \boldsymbol{L}\boldsymbol{\theta}_z \\
v(x, y) &= \boldsymbol{N}\boldsymbol{v} + \boldsymbol{M}\boldsymbol{\theta}_z \\
w(x, y) &= \boldsymbol{N}\boldsymbol{w} - \boldsymbol{L}\boldsymbol{\theta}_x - \boldsymbol{M}\boldsymbol{\theta}_y \\
\theta_x(x, y) &= \boldsymbol{N}\boldsymbol{\theta}_x \\
\theta_y(x, y) &= \boldsymbol{N}\boldsymbol{\theta}_y
\end{aligned}
\tag{17}
$$

with $\boldsymbol{u}$, $\boldsymbol{v}$, $\boldsymbol{w}$ the nodal translations and $\boldsymbol{\theta}_x$, $\boldsymbol{\theta}_y$, $\boldsymbol{\theta}_z$ the corresponding rotations (where $\boldsymbol{\theta}_z$ are the drilling rotations). The strain-displacement relations can be derived as:

$$
\begin{bmatrix} \varepsilon_x \\ \varepsilon_y \\ \gamma_{xy} \end{bmatrix} = \boldsymbol{e}(\boldsymbol{u}^{(e)}) + z\boldsymbol{k}(\boldsymbol{u}^{(e)}) = \boldsymbol{B}_m\boldsymbol{u}^{(e)} + z\boldsymbol{B}_b\boldsymbol{u}^{(e)}
\tag{18}
$$

$$
\begin{bmatrix} \gamma_{xz} \\ \gamma_{yz} \end{bmatrix} = \boldsymbol{g}(\boldsymbol{u}^{(e)}) = \boldsymbol{B}_s\boldsymbol{u}^{(e)}
\tag{19}
$$

where the element degrees of freedom vector $\boldsymbol{u}^{(e)}$ is built as $\boldsymbol{u}^{(e)} = [\boldsymbol{u}_1^{(e)}\,\boldsymbol{u}_2^{(e)}\,\boldsymbol{u}_3^{(e)}\,\boldsymbol{u}_4^{(e)}]^\top$ with $\boldsymbol{u}_i^{(e)} = [u_i\ v_i\ w_i\ \theta_{xi}\ \theta_{yi}]^\top$ defining the nodal degrees of freedom. The explicit expressions of the interpolation matrices $\boldsymbol{N}$, $\boldsymbol{L}$, $\boldsymbol{M}$ and the strain-displacement matrices $\boldsymbol{B}_m$, $\boldsymbol{B}_b$, and $\boldsymbol{B}_s$ are stated in [12].

Once the strain-displacement matrices have been defined, the expressions of the strain measures in function of the nodal degrees of freedom can be substituted in the error functional, and the resulting relation has to be minimized with respect to $\boldsymbol{u}^{(e)}$:

$$
\frac{\partial \Phi^{(e)}(\boldsymbol{u}^e)}{\partial \boldsymbol{u}^{(e)}} = 0 \quad \Rightarrow \quad \boldsymbol{K}^{(e)}\boldsymbol{u}^{(e)} = \boldsymbol{f}^{(e)}
\tag{20}
$$

where:

$$
\boldsymbol{K}^{(e)} = \frac{1}{A^{(e)}} \iint_{A^{(e)}} \left[w_e\boldsymbol{B}_m^\top\boldsymbol{B}_m + w_k h^2\boldsymbol{B}_b^\top\boldsymbol{B}_b + w_g\boldsymbol{B}_s^\top\boldsymbol{B}_s \right] \mathrm{d}A^{(e)}
\tag{21}
$$

$$
\boldsymbol{f}^{(e)} = \frac{1}{A^{(e)}} \iint_{A^{(e)}} \left[w_e\boldsymbol{B}_m^\top\boldsymbol{e}^\varepsilon + w_k h^2\boldsymbol{B}_b^\top\boldsymbol{k}^\varepsilon + w_g\boldsymbol{B}_s^\top\boldsymbol{g}^\varepsilon \right] \mathrm{d}A^{(e)}
\tag{22}
$$

It is observed that, in case of sparse strain measurements, iFEM tends to give stiff deflections resulting in a poor reconstruction.

As an example, consider a simple cantilever plate 100×50 mm, 1 mm thick, made from aluminum ($E = 70$ GPa) and under uniform pressure of 0.01 MPa, shown in Figure 5. Distributing the sensors along the bottom edge leads to an accurate deflection reconstruction, shown in Figure 6. However, if a more sparse configuration is chosen, the results quickly deteriorate, as shown in Figure 7. A much better reconstruction can be achieved pre-extrapolating the strain field, such that every inverse element has either a real or a fictitious strain measurement, thus leading to the technique explained in the next section.
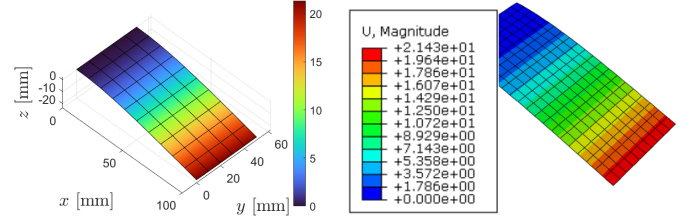
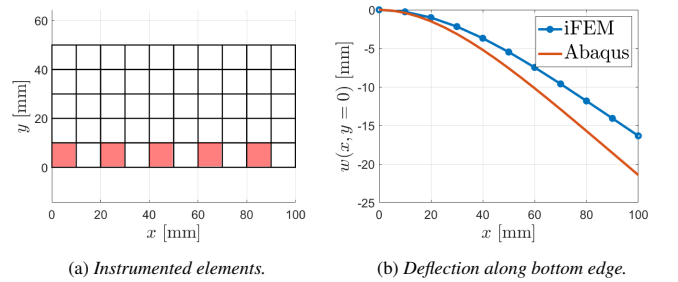(a) *Shape reconstruction with iFEM.*   (b) *Direct FEM with* `Abaqus`.

Figure 5: *Comparison of the results between iFEM and direct FEM.*
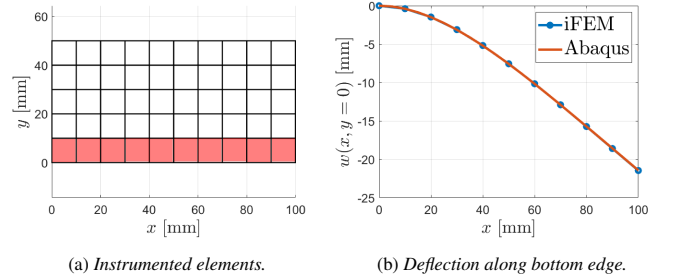
(a) *Instrumented elements.*   (b) *Deflection along bottom edge.*

Figure 6: *Bending deflection reconstruction with iFEM applying the sensors along the entire bottom edge.*

(a) *Instrumented elements.*   (b) *Deflection along bottom edge.*

Figure 7: *Bending deflection reconstruction with iFEM with a sparser sensor configuration.*

3.3. Smoothing Element Analysis

The Smoothing Element Analysis (SEA) is a technique generally applied [16, 6, 17, 5] to smoothen discrete data over a certain domain. Initially, the method was mainly devised in order to recover C^1 continuous stresses from the output of Finite Element simulations so that posteriori error estimates

were possible. However, the method is applicable to any scalar field that needs to be interpolated over a domain. The main advantage of SEA is that it uses the same framework of FEM, making SEA versatile and applicable to geometries of any form.

The procedure followed resembles the aforementioned iFEM, where here the aim is also to minimize an error functional that is expressed for an element (e) as:

$$\Phi^{(e)} = \overbrace{\frac{1}{N}\sum_{i=1}^{n^{(e)}}[\varepsilon_i^\varepsilon - \varepsilon(\boldsymbol{x}_i)]^2}^{\Phi_\varepsilon} +$$
$$+ \overbrace{\alpha \iint_{A^{(e)}}\left[\left(\frac{\partial\varepsilon}{\partial x} - \psi_x\right)^2 + \left(\frac{\partial\varepsilon}{\partial y} - \psi_y\right)^2\right]\mathrm{d}A^{(e)}}^{\Phi_\alpha} +$$
$$+ \overbrace{\beta A^{(e)} \iint_{A^{(e)}}\left[\left(\frac{\partial\psi_x}{\partial x}\right)^2 + \left(\frac{\partial\psi_y}{\partial y}\right)^2 + \frac{1}{2}\left(\frac{\partial\psi_x}{\partial y} + \frac{\partial\psi_y}{\partial x}\right)^2\right]\mathrm{d}A^{(e)}}^{\Phi_\beta}$$

(23)

Three terms build up the functional $\Phi^{(e)}$:

Φ_ε) The first term represents the squared error between the smoothed field $\varepsilon(\boldsymbol{x})$ (computed at the sampled point i) and the sampled field $\varepsilon_i^\varepsilon$ (which represents the experimental strain value). The variable N stands for the total input strains and is introduced simply as a normalization parameter, while $n^{(e)}$ is the number of strain measurements inside the element domain.

Φ_α) The second term represents a penalty factor whose weight is tuned by the scalar parameter α. In this term $\partial\varepsilon/\partial x$, $\partial\varepsilon/\partial y$ represent the derivatives of the strain field with respect to the Cartesian reference system used, while ψ_x, ψ_y are independent variables corresponding to the derivatives of the smoothed field (function of the nodal degrees of freedom). As it is possible to see, for large values of α a C^1 field is obtained since:

$$\psi_x \to \frac{\partial\varepsilon}{\partial x}; \quad \psi_y \to \frac{\partial\varepsilon}{\partial y}$$

Φ_β) The third term contains the derivatives of ψ_x, ψ_y that represent the curvatures of the smoothed field. Therefore, this term imposes a constraint on the curvature of the field whose severity is governed by the magnitude of β. For example, as stated in Tessler et al. (1998) [6], if the sampled data $\varepsilon_i^\varepsilon$ is affected by a substantial error, then larger values of β should be used to further smoothen the scalar field. As also reported in Oboe et al. (2021) [4], its influence is however much less important than the one of α and in this study a value equal to 10^{-4} is used unless otherwise specified.

After having defined the functional to be minimized, a similar framework of FEM can be set up in order to find a proper solution. The maximum derivative appearing in $\Phi^{(e)}$ is of order one,

therefore a C^0 continuous shape functions can be used to interpolate ε, ψ_x and ψ_y. In particular, for SEA a three-node element is developed using the same shape functions of the three-node inverse element named iMIN3 and described in Tessler et al. (2011) [18]. Substituting the shape functions in the functional $\Phi^{(e)}$ and minimizing w.r.t. the degrees of freedom $\boldsymbol{u}^{(e)}$ it is possible to derive a linear system of equations as:

$$(\boldsymbol{K}_\varepsilon + \boldsymbol{K}_\alpha + \boldsymbol{K}_\beta)\boldsymbol{u}^{(e)} = \boldsymbol{f}_\varepsilon \tag{24}$$

which can be assembled following the usual rules of the standard FEM. The explicit expressions of $\boldsymbol{K}_\varepsilon$, $\boldsymbol{K}_\alpha$, $\boldsymbol{K}_\beta$ and $\boldsymbol{f}_\varepsilon$ for the three-node element can be found in Oboe at al. (2021) [4]. It is important to highlight that a set of boundary conditions is not mandatory in this case, given that contrarily to FEM the functional to minimize simply represents an error w.r.t. the measurements and not the Total Potential Energy of the system.

In order to show a small application, consider again the clamped plate analyzed with iFEM in the previous section using the sparse strain sensor configuration (Figure 7a). Now this study case is analyzed again introducing first the strain pre-extrapolation with SEA. The SEA mesh can be seen in Figure 8a together with the positions where the strain is sampled from the FEM model. Note that additional strain sensors have been put at the upper edge basically because otherwise SEA would result in an ill-conditioned system of equations. Solving the SEA linear system for the axial strain ε_x results in the strain field over the full structural domain as shown in Figure 8b. In summary every iFEM element (mesh cf. Figure 8c) obtains as input a strain value either real (red in Figure 8c) or fictitious from SEA (blank in Figure 8c). Computing the resulting deformations with iFEM as explained before results in the bending displacement reported in Figure 8d.
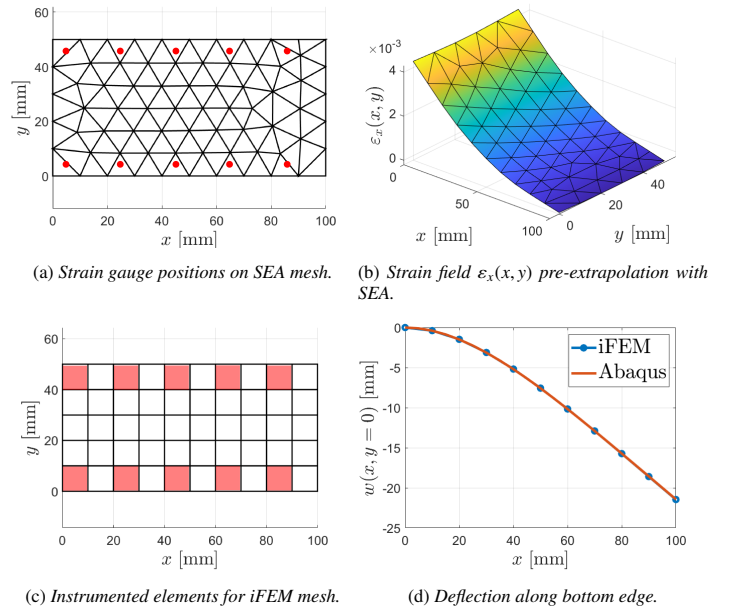

(a) *Strain gauge positions on SEA mesh.*

(b) *Strain field $\varepsilon_x(x, y)$ pre-extrapolation with SEA.*

(c) *Instrumented elements for iFEM mesh.*

(d) *Deflection along bottom edge.*

Figure 8: *iFEM results and comparison with direct FEM.*

4. Strain per-extrapolation for wing-like structures

The application of SEA for relatively complex geometries, such as the skin of the wing introduced in Section 2, creates some additional complexities compared to the studies reported in literature so far [4, 16] and the results generally depend on two scalar parameters which have to be given as input: the drilling stiffness k_{ψ_z} and the SEA parameter α. It is important to understand the dependency of the results on these parameters.

The SEA described in Section 3 has been only applied for two-dimensional problems in the literature, e.g. in Oboe et al. [4], or in three-dimensional structural elements made from flat plates where SEA could be applied separately in each plate [16]. For more complex geometries, like the skin of wing-like structures, there is the need to add a "drilling" degree of freedom to enable a proper connection amongst the three-dimensional plates, while allowing an adequate transformation of all rotations from the individual element coordinate system to the global coordinate system. For the present work, a fictitious drilling stiffness k_{ψ_z} is added to each node such that in the local reference system $k_{\psi_z}\psi_z = 0$, with ψ_z the variable analogous to ψ_x and ψ_y in the previously introduced formulation. The effect of this parameter is discussed next.

Regarding the influence of the parameter α, it should be tuned such that a good compromise between the two terms Φ_ε and Φ_α is reached. Here, a simple method sometimes followed in the solution of least-squares problems is applied [19], which consists of the residual Φ_ε plotted over Φ_α in a log-log plot, for different values of α. This plot results in a curve that generally shows a distinct corner, from which the parameter α is chosen. The method is intuitive and simple to implement, but heuristic, meaning that there is no theoretical guarantee that at the corner of the residuals curve the error w.r.t. the reference strain field is minimized. On that account the choice of the regularization parameter will be checked computing the error of the pre-extrapolated strain field for different values of α.

In the following these scalar parameter are first tuned using the three-node SEA element available from literature. Next, a novel four-node element is introduced and an algorithm to speed up finding a suitable value for α is described.

4.1. SEA with three-node element

Using the triangular SEA elements, the strain field of the wing subjected to the tip load has been interpolated. With suitable parameters, a relatively good approximation can be found. For example, in Figure 9 it is shown ε_x over the wing surface using $k_{\psi_z} = 10^{-4}$ and $\alpha = 10^{-2}$. However, the results are dependent on α and k_{θ_z} in an unclear way. Using $k_{\psi_z} = 10^{-8}$ in Figure 10a the residuals are plotted for different values of α and the corresponding L2-norm error of the strain field in Figure 10b. As shown in Figure 10b, the corner of the curve (×) of the residuals does not correspond to a minimum in the error of the strain field. Furthermore, the results largely depend on different values for k_{ψ_z}, as illustrated in Figure 11.
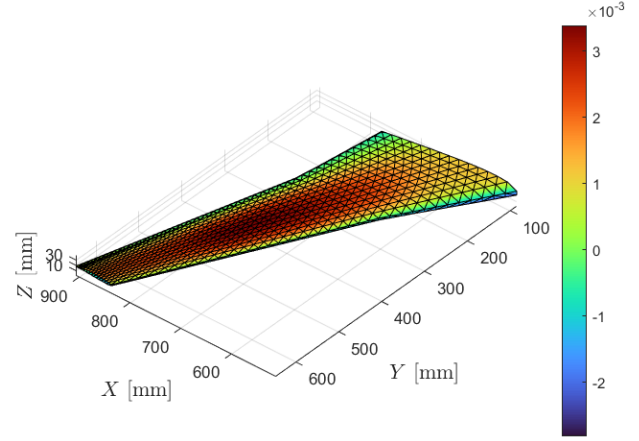
(a) *Extrapolated ε_x field over wing skin.*
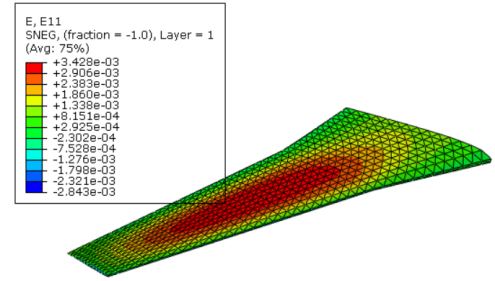
(b) *Reference ε_x field from direct FEM.*

Figure 9: *SEA with three-node elements.*

4.2. SEA with novel four-node element

Using the three-node SEA elements it is not possible to identify an optimal configuration for the parameters in order to obtain a consistent strain field from the strain measurements. Therefore, a novel four-node element is employed, which showed to perform better because of a reduced sensitivity with respect to the choice of the scalar parameters k_{ψ_z} and α. The same shape functions of the iQS4 element are used and thus the functional $\Phi^{(e)}$ reads [2]:
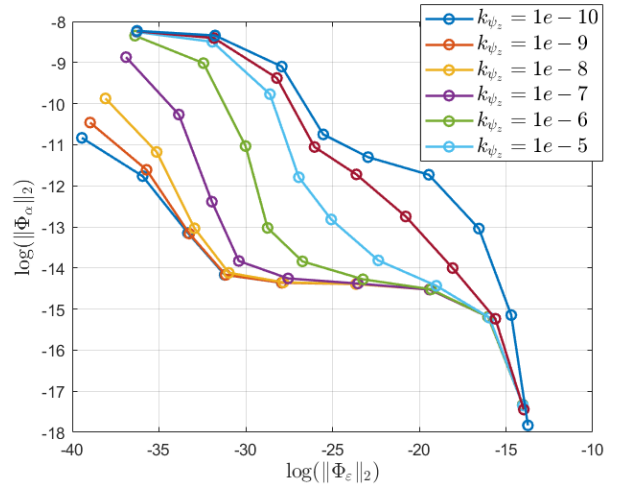
$$\Phi^{(e)} = \frac{1}{N}\sum_{i=1}^{n^{(e)}}[\varepsilon_i^\varepsilon - \varepsilon(\boldsymbol{x}_i)]^2 +$$

$$+ \alpha \iint_{A^{(e)}}\left[\left(\frac{\partial\varepsilon}{\partial x} + \psi_y\right)^2 + \left(\frac{\partial\varepsilon}{\partial y} - \psi_x\right)^2\right]dA^{(e)} +$$

$$+ \beta A^{(e)}\iint_{A^{(e)}}\left[\left(\frac{\partial\psi_x}{\partial y}\right)^2 + \left(\frac{\partial\psi_y}{\partial x}\right)^2 + \frac{1}{2}\left(\frac{\partial\psi_x}{\partial y} + \frac{\partial\psi_y}{\partial x}\right)^2\right]dA^{(e)}$$

$$(25)$$

The following analogy can be done between the displacement and strain field of the iQS4 element and the scalar field ε to be interpolated in SEA:
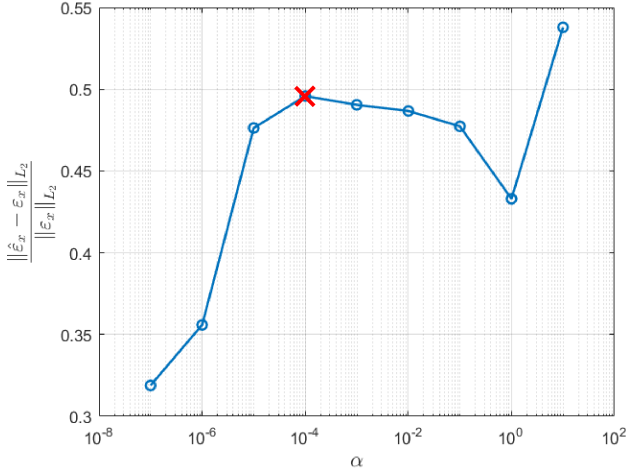
---

[2]$\Phi^{(e)}$ is slightly modified due to the different orientation of ψ_y in in the framework of the 4-noded element.
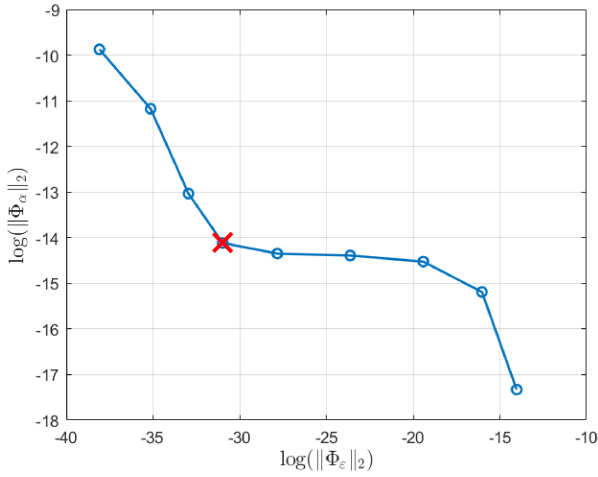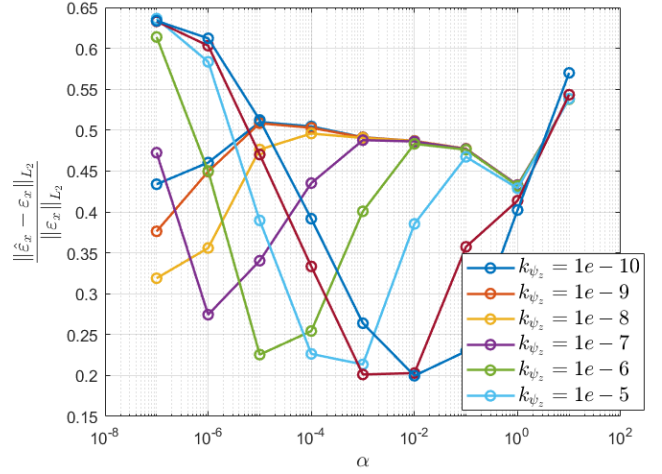
(a) *Residuals for different values of α.*

(b) *Relative L2-norm error of the strain field εx.*

Figure 10: *Example of difficulty in choosing the regularization parameter α.*

(a) *Residuals for different values of α and k_{ψ_z}.*

(b) *Relative L2-norm error of the strain field εx.*

Figure 11: *Dependence of the results in function of the drilling stiffness k_{ψ_z}.*

$$
\begin{aligned}
w &\leftrightarrow \varepsilon \\
\gamma_{xz} &\leftrightarrow \frac{\partial \varepsilon}{\partial x} + \psi_y \\
\gamma_{yz} &\leftrightarrow \frac{\partial \varepsilon}{\partial y} - \psi_x
\end{aligned}
$$

The SEA variables ε, ψ_x, ψ_y are interpolated by means of the last three equations of the displacement and strain relations described by the iQS4 element (cf. Eq.(17)):

$$
\begin{aligned}
\varepsilon &= \boldsymbol{N}s - \boldsymbol{L}s_x - \boldsymbol{M}s_y \\
\psi_x &= \boldsymbol{N}s_x \\
\psi_y &= \boldsymbol{N}s_y
\end{aligned}
\tag{26}
$$

with $\boldsymbol{N}$, $\boldsymbol{L}$, $\boldsymbol{M}$ the corresponding shape function matrices of the iQS4 element and $\boldsymbol{s}$, $\boldsymbol{s}_x$, $\boldsymbol{s}_y$ the element degrees of freedom of the SEA element. The element SEA matrices can be derived as follows:

- For the first term:

$$
\begin{aligned}
\Phi_\varepsilon &= \frac{1}{N} \sum_i [\varepsilon_i^\varepsilon - \varepsilon(\boldsymbol{u}^{(e)})]^2 \\
&= \frac{1}{N} \sum_i [\varepsilon_i^\varepsilon - \underbrace{\begin{bmatrix} \boldsymbol{N} & -\boldsymbol{L} & -\boldsymbol{M} \end{bmatrix}}_{\widetilde{\boldsymbol{N}}} \boldsymbol{u}^{(e)}]^2 \\
&= \frac{1}{N} \sum_i [(\varepsilon_i^\varepsilon)^2 + \boldsymbol{u}^{(e)\top} \widetilde{\boldsymbol{N}}^\top \widetilde{\boldsymbol{N}} \boldsymbol{u}^{(e)} - 2\varepsilon_i^\varepsilon \widetilde{\boldsymbol{N}} \boldsymbol{u}^{(e)}]
\end{aligned}
\tag{27}
$$

with $\boldsymbol{u}^{(e)} = [s\ s_x\ s_y]^\top$. Minimizing w.r.t. $\boldsymbol{u}^{(e)}$ it is possible to obtain:

$$
\boldsymbol{K}_\varepsilon \boldsymbol{u}^{(e)} = \boldsymbol{f}_\varepsilon
\tag{28}
$$

where:

$$
\boldsymbol{K}_\varepsilon = \frac{1}{N} \sum_i \widetilde{\boldsymbol{N}}^\top \tilde{\boldsymbol{N}} \quad ; \quad \boldsymbol{f}_\varepsilon = \frac{1}{N} \sum_i \varepsilon_i^\varepsilon \widetilde{\boldsymbol{N}}
\tag{29}
$$

(a) *Residuals of ε_x.*

(a) *Residuals of Φ_ε and Φ_α for different values of α.*
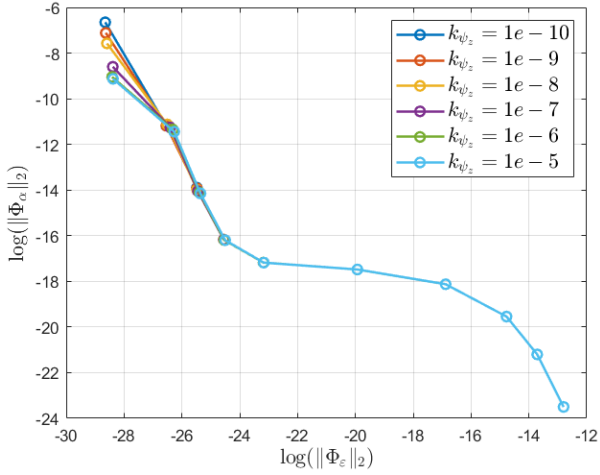
(b) *Relative L2-norm error for ε_x.*

(b) *Relative L2-norm error of ε_x strain field.*
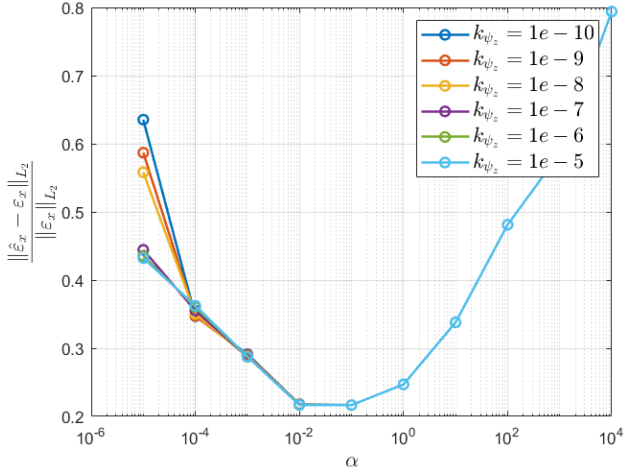
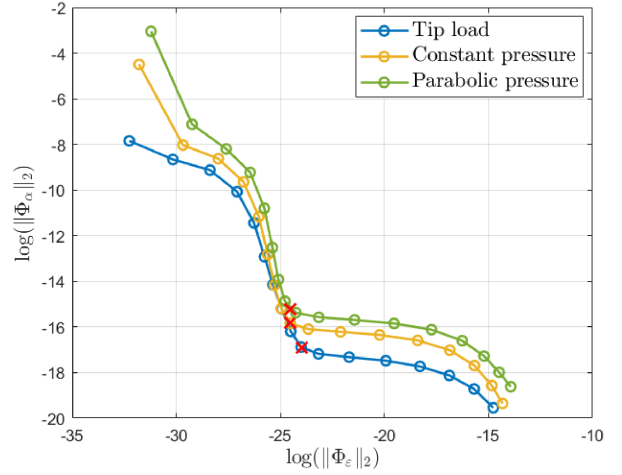Figure 12: *Dependence of the results on k_{ψ_z} for tip load case.*

Figure 13: *Interpolation of strain field ε_x with SEA for the three different load cases.*

- For the second term:

$$
\begin{aligned}
\Phi_\alpha &= \iint_{A^{(e)}} \left[\left(\frac{\partial \varepsilon}{\partial x} + \psi_y \right)^2 + \left(\frac{\partial \varepsilon}{\partial y} - \psi_x \right)^2 \right] \mathrm{d}A^{(e)} \\
&= \iint_{A^{(e)}} \left[\underbrace{\left[\frac{\partial N}{\partial x} \quad -\frac{\partial L}{\partial x} \quad \left(-\frac{\partial M}{\partial x} + N \right) \right]}_{B_1} u^{(e)} \right]^2 + \\
&\quad + \left[\underbrace{\left[\frac{\partial N}{\partial x} \quad \left(-\frac{\partial L}{\partial x} - N \right) \quad -\frac{\partial M}{\partial x} \right]}_{B_2} u^{(e)} \right]^2 \mathrm{d}A^{(e)}
\end{aligned}
\tag{30}
$$

and minimizing it is possible to obtain:

$$
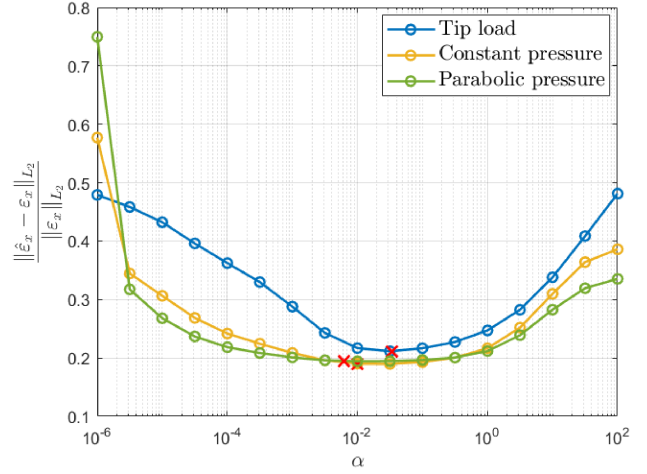K_\alpha u^{(e)} = 0
\tag{31}
$$

with:

$$
K_\alpha = \iint_{A^{(e)}} \left(B_1^\top B_1 + B_2^\top B_2 \right) \mathrm{d}A^{(e)}
\tag{32}
$$

- Finally, for the last term:

$$
\begin{aligned}
\Phi_\beta &= \iint_{A^{(e)}} \left[\left(\frac{\partial \psi_x}{\partial y} \right)^2 + \left(\frac{\partial \psi_y}{\partial x} \right)^2 + \frac{1}{2} \left(\frac{\partial \psi_x}{\partial y} + \frac{\partial \psi_y}{\partial x} \right)^2 \right] \mathrm{d}A^{(e)} \\
&= \iint_{A^{(e)}} \left[\left(\frac{\partial N}{\partial y} s_x \right)^2 + \left(\frac{\partial N}{\partial x} s_y \right)^2 + \frac{1}{2} \left(\frac{\partial N}{\partial y} s_x + \frac{\partial N}{\partial x} s_y \right)^2 \right] \mathrm{d}A^{(e)} \\
&= \iint_{A^{(e)}} \left[s_x^\top \left(\frac{\partial N}{\partial y} \right)^\top \frac{\partial N}{\partial y} s_x + s_y^T \left(\frac{\partial N}{\partial x} \right)^T \frac{\partial N}{\partial x} s_y + \right. \\
&\quad \left. + \frac{1}{2} \left(\left(\frac{\partial N}{\partial y} s_x \right)^2 + \left(\frac{\partial N}{\partial x} s_y \right)^2 + 2 \frac{\partial N}{\partial y} s_x \frac{\partial N}{\partial x} s_y \right) \right]
\end{aligned}
\tag{33}
$$

Minimizing towards all SEA element DOFs leads to:

$$
\frac{\partial \Phi_\beta}{\partial s} = 0
\tag{34}
$$

9

$$\frac{\partial \Phi_\beta}{\partial s_x} = \iint_{A^{(e)}} \left[2\left(\frac{\partial N^\top}{\partial y}\frac{\partial N}{\partial y}\right)s_x + \left(\frac{\partial N^\top}{\partial y}\frac{\partial N}{\partial y}\right)s_x + \frac{\partial N^\top}{\partial y}\frac{\partial N}{\partial x}s_y \right] dA^{(e)}$$

$$\iint_{A^{(e)}} \left[0 \quad \left(\frac{\partial N^\top}{\partial y}\frac{\partial N}{\partial y} + \frac{1}{2}\frac{\partial N^\top}{\partial y}\frac{\partial N}{\partial y}\right) \quad \frac{1}{2}\frac{\partial N^\top}{\partial y}\frac{\partial N}{\partial x} \right] u^{(e)} dA^{(e)} \tag{35}$$

$$\frac{\partial \Phi_\beta}{\partial s_y} = \iint_{A^{(e)}} \left[2\left(\frac{\partial N^\top}{\partial x}\frac{\partial N}{\partial x}\right)s_y + \left(\frac{\partial N^\top}{\partial x}\frac{\partial N}{\partial x}\right)s_y + \frac{\partial N^\top}{\partial y}\frac{\partial N}{\partial x}s_x \right] dA^{(e)}$$

$$\iint_{A^{(e)}} \left[0 \quad \frac{1}{2}\frac{\partial N^T}{\partial y}\frac{\partial N}{\partial x} \quad \left(\frac{\partial N^\top}{\partial x}\frac{\partial N}{\partial x} + \frac{1}{2}\frac{\partial N^\top}{\partial x}\frac{\partial N}{\partial x}\right) \right] u^{(e)} dA^{(e)} \tag{36}$$

And so:

$$K_\beta u^{(e)} = 0 \tag{37}$$

with:

$$K_\beta = \iint_{A^{(e)}} \begin{bmatrix} 0 & 0 & 0 \\ 0 & \frac{3}{2}\frac{\partial N^\top}{\partial y}\frac{\partial N}{\partial y} & \frac{1}{2}\frac{\partial N^T}{\partial y}\frac{\partial N}{\partial x} \\ 0 & \frac{1}{2}\frac{\partial N^\top}{\partial y}\frac{\partial N}{\partial y} & \frac{3}{2}\frac{\partial N^\top}{\partial x}\frac{\partial N}{\partial x} \end{bmatrix} dA^{(e)} \tag{38}$$

In assembling the matrices K_ε, K_α, K_β it is important to remember to add the degree of freedom ψ_z with a corresponding drilling stiffness k_{ψ_z}.

The element type introduced above is adopted to discretize the wing, which is analyzed for the three load cases (cf. Fig. 3). It is possible to see that a value close to the optimum can be found at the corner of the residual curve (identified by × in Figure 13a). This point is found from the minimum curvature of the curve: the various sampled points are interpolated by cubic splines, from which the curvature can be analytically computed (using Eq.(39)). Its minimum value gives the location of the desired point. In Figure 13b the corresponding relative L2-norm error for the strain component ε_x is plotted. The highlighted point (×) represents the value of α where the highest curvature of the residuals curve occurs. Note that the identified point is in general close to the actual optimum point. Regarding the sensitivity on the choice for k_{ψ_z}, a lower dependence on this parameter can be verified. For example, in the case of ε_x for the tip load case, the graphs of Figure 12 can be obtained. There is an almost perfect overlap for the different values of k_{ψ_z} apart from very low values of α, which in any case are far from the corner of the residual curve.

4.3. Algorithm to quickly find the optimal value of α

It is possible to develop a simple algorithm in order to find the corner of the residual curve, similarly to what is proposed in Hansen et al. (1993) [20]. This would allow on one side to automate the process without any user intervention, and on the other one to lower the number of evaluations needed to find the optimum value of α. Suppose that some points have been sampled using different values of α and that the corner is inside the identified range (from the minimum to the maximum value of α used). Furthermore, let $\eta = \log(\Phi_\varepsilon)$ and $\rho = \log(\Phi_\alpha)$. Then it is possible to follow the algorithm below:
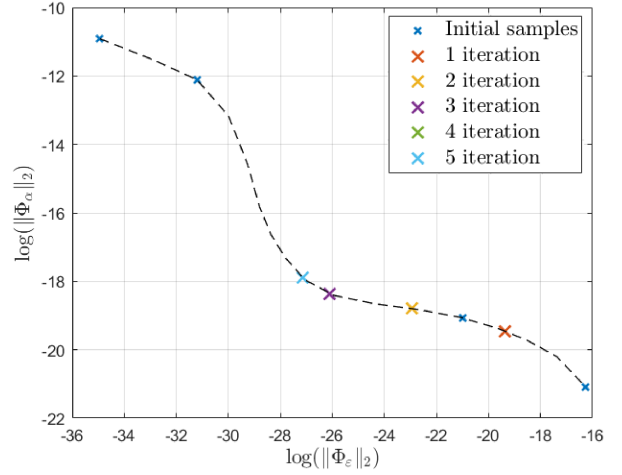
(a) *Iterations on the residual curve.*
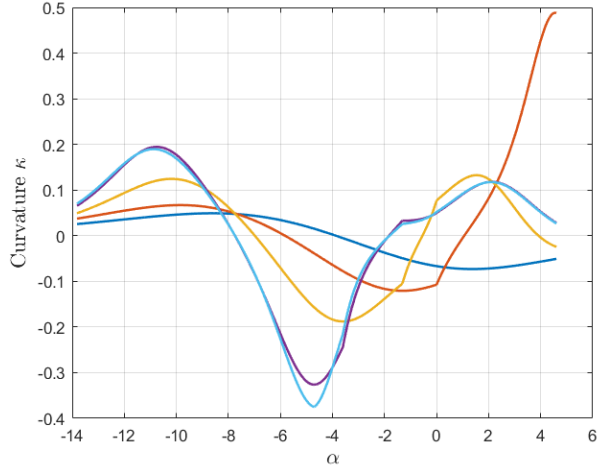
(b) *Curvature $\kappa(\alpha)$ for the different iterations.*

Figure 14: *Example of the applicability of the algorithm to retrieve a suitable value of α in a few iterations.*

1. Interpolate with cubic splines the points (η_i, α_i) and (ρ_i, α_i) such that the expressions of $\rho = \rho(\alpha)$ and $\eta = \eta(\alpha)$ are available.

2. Compute the maximum curvature κ of the interpolated residual curve from:

$$\kappa(\alpha) = \frac{\rho'\eta'' - \rho''\eta'}{((\rho')^2 + (\eta')^2)^{3/2}} \quad \text{with} \quad \bullet' = d/d\alpha \tag{39}$$

3. Use the value of α found for the maximum curvature point to evaluate the residuals ρ and η at that point.

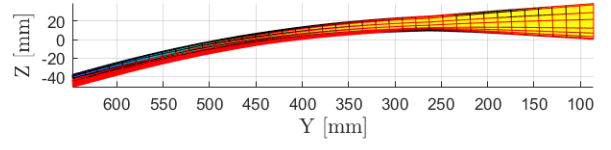4. Repeat from (1) until convergence.

As an example, for the case of a tip load and considering the measurement of γ_{xy}, the algorithm starts with 4 initial guesses. From these, convergence is reached after 5 iterations, as shown in Figure 14. Compared to Figure 13a, it is possible to obtain a good estimate of α with a considerably smaller number of evaluations.
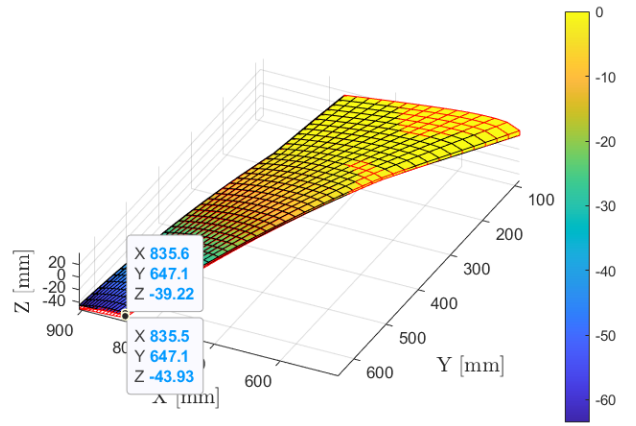
10
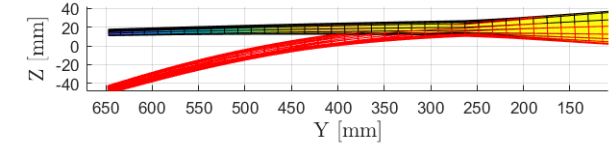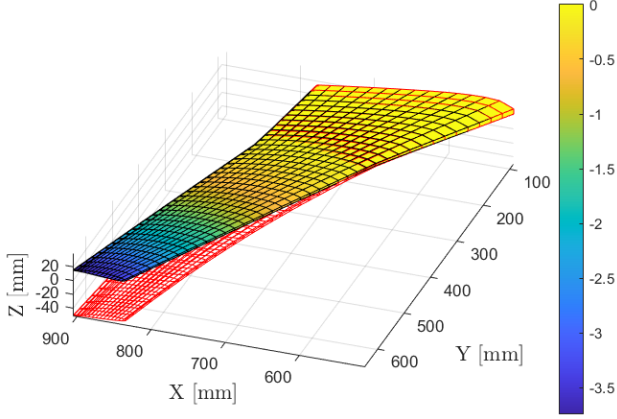
(a) *Front view.*

(b) *Isometric view.*

Figure 15: *Comparison of reconstructed and reference (red mesh) deflection for tip load case with the direct application of iFEM.*

5. Shape sensing with SEA and iFEM

The results obtained from SEA are now exploited as input for iFEM to reconstruct the wing deflection. Before proceeding, two points are highlighted:

- Only the strains on the upper surface are considered. With no information of the curvature of the shell, it is assumed that the inverse shell elements are subjected mainly to membrane strains. This is consistent with the fact that the wing is a beam-like structure [3]. Therefore, the vector of experimental curvatures $\boldsymbol{k}^\varepsilon$ is assumed to be null.

- The strain is virtually measured according to the material reference system, as if the strain rosettes were aligned with the direction of the outer ply. So, it is necessary to rotate the measured strain in the local element reference system, defined as:

$$\boldsymbol{n} = \frac{\boldsymbol{X}_{31} \times \boldsymbol{X}_{42}}{\|\boldsymbol{X}_{31} \times \boldsymbol{X}_{42}\|} \quad ; \quad \boldsymbol{e}_1 = \frac{\boldsymbol{X}_{31} + \boldsymbol{X}_{24}}{\|\boldsymbol{X}_{31} + \boldsymbol{X}_{24}\|} \quad ; \quad \boldsymbol{e}_2 = -\boldsymbol{e}_1 \times \boldsymbol{n}$$

where $\boldsymbol{X}_{ij} = \boldsymbol{X}_i - \boldsymbol{X}_j$, with $\boldsymbol{X}_i$, $\boldsymbol{X}_j$ the nodal positions in the global reference system. So the transformation matrix is $\boldsymbol{T} = \begin{bmatrix} \boldsymbol{e}_1 & \boldsymbol{e}_2 & \boldsymbol{n} \end{bmatrix}^\top$ which can be applied to the element matrices before assembly. The measured strain can be rotated in the element reference system in the usual way:

$$\begin{bmatrix} \varepsilon_x \\ \varepsilon_y \\ \gamma_{xy} \end{bmatrix} = \begin{bmatrix} \cos^2\theta & \sin^2\theta & \sin\theta\cos\theta \\ \sin^2\theta & \cos^2\theta & -\sin\theta\cos\theta \\ -2\sin\theta\cos\theta & 2\sin\theta\cos\theta & \cos^2\theta - \sin^2\theta \end{bmatrix} \begin{bmatrix} \varepsilon_x^\varepsilon \\ \varepsilon_y^\varepsilon \\ \gamma_{xy}^\varepsilon \end{bmatrix} \tag{40}$$

(a) *Front view.*

(b) *Isometric view.*

Figure 16: *Comparison of reconstructed and reference (red mesh) deflection for tip load case pre-extrapolating the strain field with SEA before applying iFEM.*

with $[\varepsilon_x^\varepsilon \ \varepsilon_y^\varepsilon \ \gamma_{xy}^\varepsilon]^\top$ the measured strains, $[\varepsilon_x \ \varepsilon_y \ \gamma_{xy}]^\top$ the ones in the local element reference system and θ the angle between the two reference systems.

Load case	$\dfrac{\|\hat{w} - w\|_{L_2}}{\|w\|_{L_2}}$
Tip load	0.0195
Constant pressure	0.0166
Parabolic pressure	0.014

Table 3: *Relative L2-norm error of the vertical displacement field w.r.t. the reference solution for three different load cases.*

In order to assess the error of the iFEM model, first the full strain field from the direct FEM analysis will be used as input. That is, to every inverse element it is given as input the actual strain field to determine the maximum attainable accuracy of the shape sensing scheme. This procedure is repeated for all three load cases, obtaining the relative L2-norm error between estimated ($\hat{w}$) and reference (w) vertical displacements as in Table 3. A good reconstruction of the deflection is obtained, and three sources of error are identified:

- The discretization in inverse FE.

- The assumption that the skin undergoes only membrane strains, with no curvature.

- Finally, it is important to recall that the elements used (iQS4) are based on the simple First Order Shear Deformation theory. The wing is made from a stiff outer skin, but also the in-

11

ner presence of the foam material has some influence. However, due to the very low elastic modulus of the foam compared to the outer skin, the usage of iQS4 elements seems to be a suitable choice also for this study case.

Having evaluated the minimum error assuming one sensor per inverse element, the following study limits the strain measurements to the configuration illustrated in Figure 1b. First, iFEM is directly applied with a weight of $w_e, w_k, w_g = 10^{-4}$ for the strainless elements, leading to a poor reconstruction of the deflection, as depicted in Figure 15. Here, the reference deflection extracted from the direct FEM simulation is also plotted and it is possible to compute a relative L2-norm error of the vertical displacement equal to 0.941. The deformation predicted in general underestimates the true displacements, as similarly observed for the clamped plate example of Section 3. To overcome the stiff deformed shape obtained with the direct use of iFEM, it is proposed the pre-extrapolation of the strain field using SEA before applying iFEM. The optimal value of α is found at the corner of residual error curve (Figure 13a). Next, a full strain field is generated with SEA, and then applied to iFEM, again using a weight of 10^{-4} for the strainless elements. The results are presented in Figure 16. A relative L2-norm error of 0.073 is computed w.r.t the reference displacement along z. There is a significant improvement compared to the case without the strain pre-extrapolation. Furthermore, with view on Table 3, the result is relatively close to the best possible estimate. To gain more insight into the influence of both the SEA coefficient α and the weight assigned to strainless elements on the outcome, their impact is investigated in the following.

5.1. Influence of weight given to strainless elements

It is often found in literature [12, 13, 3, 14, 15] the statement that inverse elements without strain information should be given a lower weight in the minimization of the error functional. This approach leads supposedly to more accurate predictions because higher importance is accounted to the minimization of the error of the actual strain measurements. However, considering that the strainless elements are fictitiously instrumented by SEA, the membrane strains and curvatures can be estimated, but these strain values given as input to the inverse elements are in general approximations of the true strain field and, therefore, it is useful to understand how the choice of the weights w_e and w_k affects the final results. The weight related to the transverse shear strain w_g on the contrary is assumed to be constant and small since SEA does not allow to obtain an estimate for it. The displacement of the wing has been recovered for all load cases with iteratively varying the value of the weights. In particular, for w_g a low value of 10^{-5} is used, while the value for w_e and w_k is altered as displayed in Figure 17 where the error of the reconstructed displacement field is shown. Starting from very large values, the reduction of the weights leads in a first step to an improvement of the overall solution. This can be explained because the minimization of the functional allows to better match the "real" strain measurements. However, at some point the error starts to rise again: very low weights used

for strainless elements result in an ill-conditioned linear system which reduces the accuracy of the solution. In any case, the range of weight values that can be used for the strainless elements is sufficiently broad, and is consistent with what is usually suggested in the literature ($\approx 10^{-4}$). In the following analysis, a weight of 10^{-4} is used, unless otherwise specified.
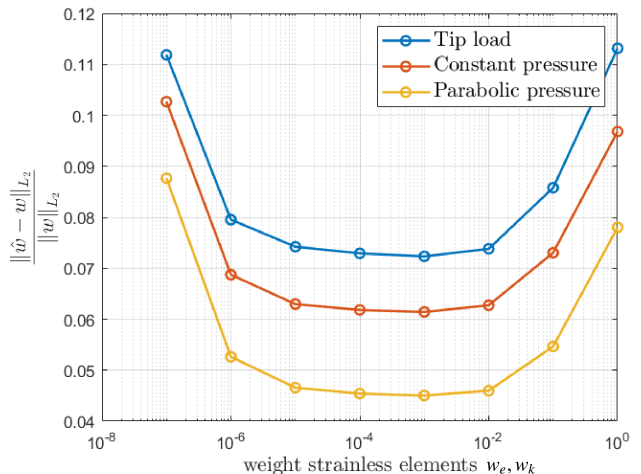

Figure 17: *Influence of weights given to strainless elements on the displacement reconstruction.*
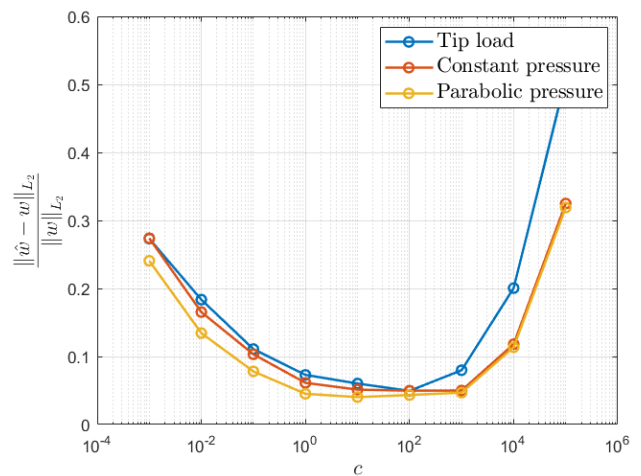

Figure 18: *Influence of SEA parameter α on the displacement reconstruction.*

5.2. Influence of SEA α coefficient on iFEM

It is also important to assess how the choice of the regularization parameter α influences the iFEM reconstruction of the displacement field. Therefore, a few parametric studies have been carried out as illustrated in Figure 18 where the relative displacement field error is plotted versus different values of the SEA parameter α. The identified optimum values of α_{opt} from SEA have been replaced by the quantity $c\,\alpha_{opt}$, with the coefficient c displayed on the x axis.

The plot shows a relatively flat region towards the minimum, meaning that, at least in that region, the results are quite insensitive on the choice of α. This is especially true for the range higher than the identified optimum values of α ($1 < c < 10^3$).
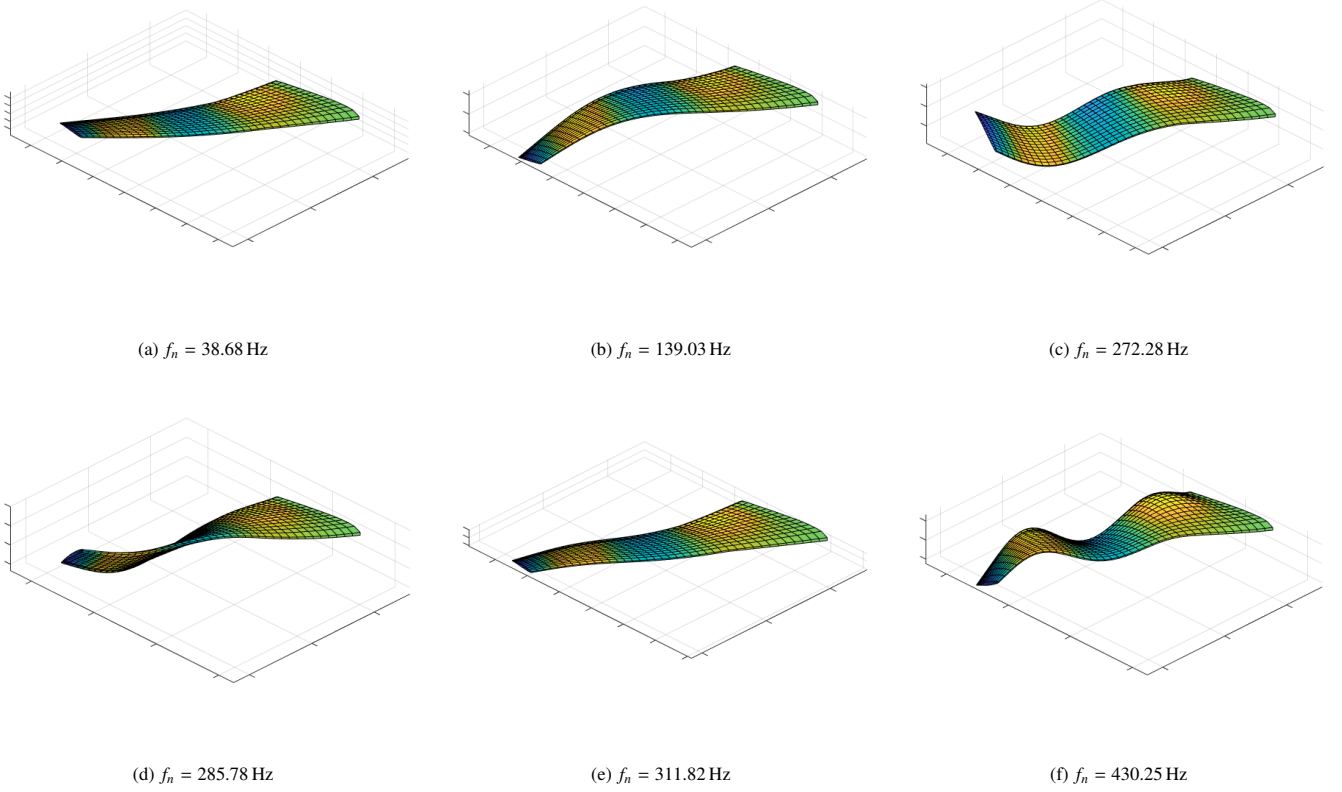
(a) $f_n = 38.68$ Hz

(b) $f_n = 139.03$ Hz

(c) $f_n = 272.28$ Hz

(d) $f_n = 285.78$ Hz

(e) $f_n = 311.82$ Hz

(f) $f_n = 430.25$ Hz

Figure 19: *First six modes of the wing and corresponding natural frequencies f_n.*

6. Comparison between iFEM and Modal Method

In the following implementation of the Modal Method, the first six vibration modes of the structure are assumed to be sufficient to reconstruct the deformed shapes. They are shown in Figure 19 together with the corresponding natural frequencies. From the seventh mode onward, the observed modes become more shell-related and are neglected in the shape reconstruction.

Since the deformation of the wing is dominated by bending, the first few modes have the highest importance in reconstructing the displacement field. However, it is also seen that mode 6 slightly contributes to the shape sensing analysis. A quantitative method to assess the number of modes required in the shape sensing analysis was proposed by Bogert et al. (2003) [2], using a reference static deformed shape U. Knowing that in general $U = \mathbf{\Phi} r$ with r the modal coordinates and $\mathbf{\Phi}$ the mode shape matrix, then:

$$r = (\mathbf{\Phi}^\top \mathbf{\Phi})^{-1} \mathbf{\Phi}^\top U \tag{41}$$

which are the modal coordinates that can best represent, in a least-square sense, the static deformed shape. Now, the strain energy of the i mode shape is given by:

$$E_i = \frac{1}{2}(\mathbf{\Phi}_i r_i)^\top K(\mathbf{\Phi}_i r_i) = \frac{1}{2} r_i^T \mathbf{\Phi}_i^\top K(\mathbf{\Phi}_i r_i) \tag{42}$$

with r_i the ith modal coordinate and $\mathbf{\Phi}_i$ the ith mode shape. Comparing E_i to the strain energy due to the reference static deformation given by:

$$E = \frac{1}{2} U^\top K U \tag{43}$$

it is possible to assess the weight of each mode in the final shape sensing result. Of course, in general U is not known (otherwise there would be no reason to carry out the shape sensing study) and just an estimate can be used. In the following, however, the reference deformed shape from FEM is directly employed for U. Only reporting the results for the tip load case, in Figure 20a it is shown the relative strain energy contribution of each mode. Figure 20b displays the relative L2-norm error of the vertical displacement field w in function of the number of modes used for the three load cases, together with the one obtained from iFEM. The Modal Method generally performs better when compared to iFEM, even though the results are load case dependent. Furthermore, no uncertainties are introduced in the system, which is evaluated next in the present study during a comparison on how iFEM performs w.r.t. the Modal Method in terms of the sensitivity of the methods towards uncertainties.
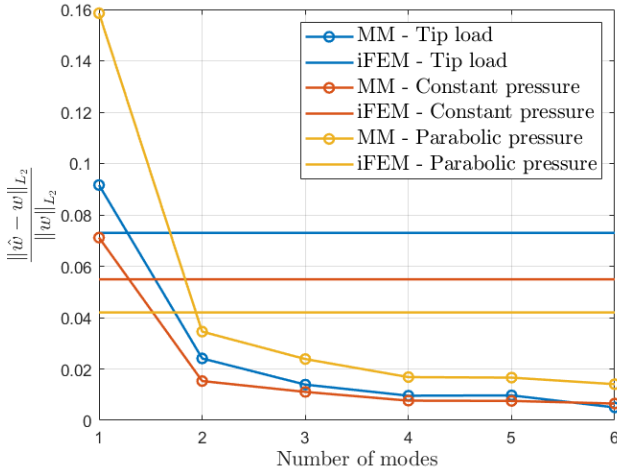
7. Uncertainty Quantification

With the aim to assess the influence of uncertainties on the shape sensing analysis, a Gaussian probability density function is assumed for the input variables and a Monte Carlo simulation is carried out, where each input is randomly sampled with the
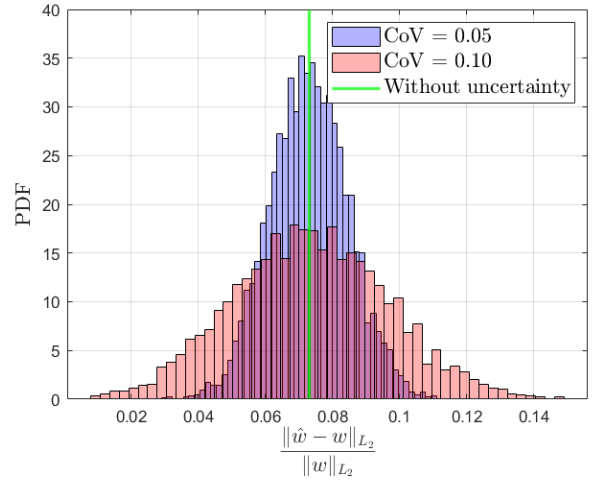
13
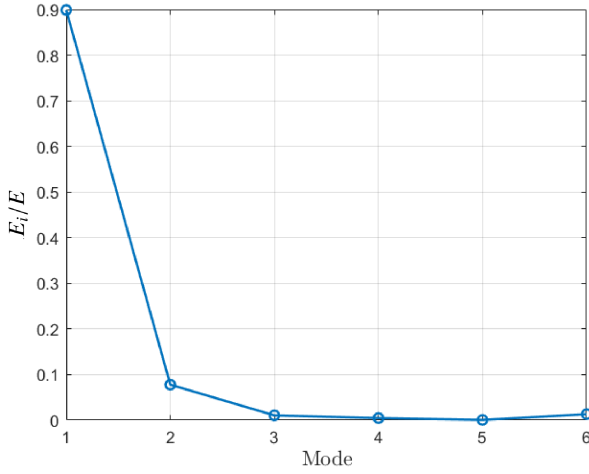
(a) *Mode strain energy for tip load case.*
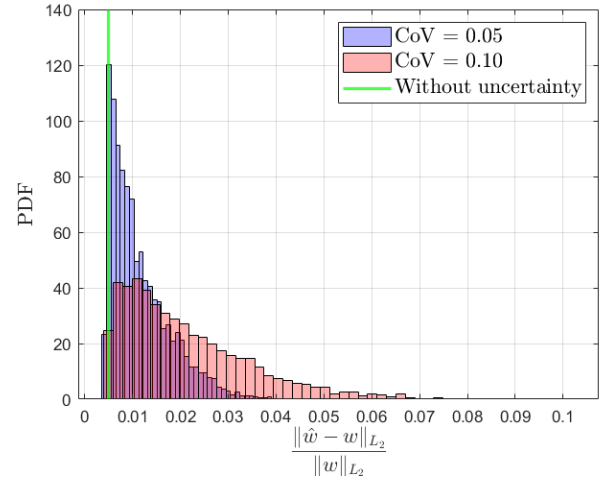
(b) *Shape sensing error for tip load case.*

Figure 20: *Shape sensing with Modal Method for three different load cases and comparison with iFEM.*

(a) *MM.*

(b) *iFEM.*

Figure 21: *Probability density function (PDF) of relative L2-norm error of vertical displacement estimated with Monte Carlo Simulation for tip load in case of measurement uncertainty.*

Latin Hypercube Sampling and the deterministic output for the randomly generated configuration is computed. The end result is a distribution of reconstructed shapes, being each one evaluated with the L2-error norm of the reconstructed displacement w.

The input variables for the present Monte Carlo simulation depend on the shape sensing scheme used. Since iFEM is solely based on strain-displacement relations, it is only affected by possible measurement errors, whereas the Modal Method is also affected by the uncertainties related to the material properties, because in this case the vibration mode shapes need to be calculated. In the following, these two types of uncertainties are studied separately, respectively in subsections 7.1 (measurement uncertainty) and 7.2 (material uncertainty). A similar study can be found in Esposito et al. (2021) [13], where iFEM and MM are also compared. However, in [13] the sensor positions have been optimized for each method based on the applied load, resulting in a relatively high number of measure-

ments. Furthermore, no strain pre-extrapolation is carried out for iFEM, making the two studies relatively different, both in the inputs given and in the output which will be observed.

The present Uncertainty Quantification study is carried out with the help of UQLab, a MATLAB toolbox for uncertainty quantification [21].

7.1. Measurement Uncertainty

The strain measurements are assumed to be affected by an error normally distributed, with mean μ being the deterministic measurement value. Two simulations are carried out increasing the variance from $5\%\mu$ to $10\%\mu$, resulting in Coefficients of Variation (CoV= σ/μ) of respectively 0.05 and 0.1. The resulting PDFs are reported in Figure 21a (MM) and Figure 21b (iFEM) using $5\,10^3$ samples for each simulation which enabled to reach a converged distribution. Only the results for the tip load case
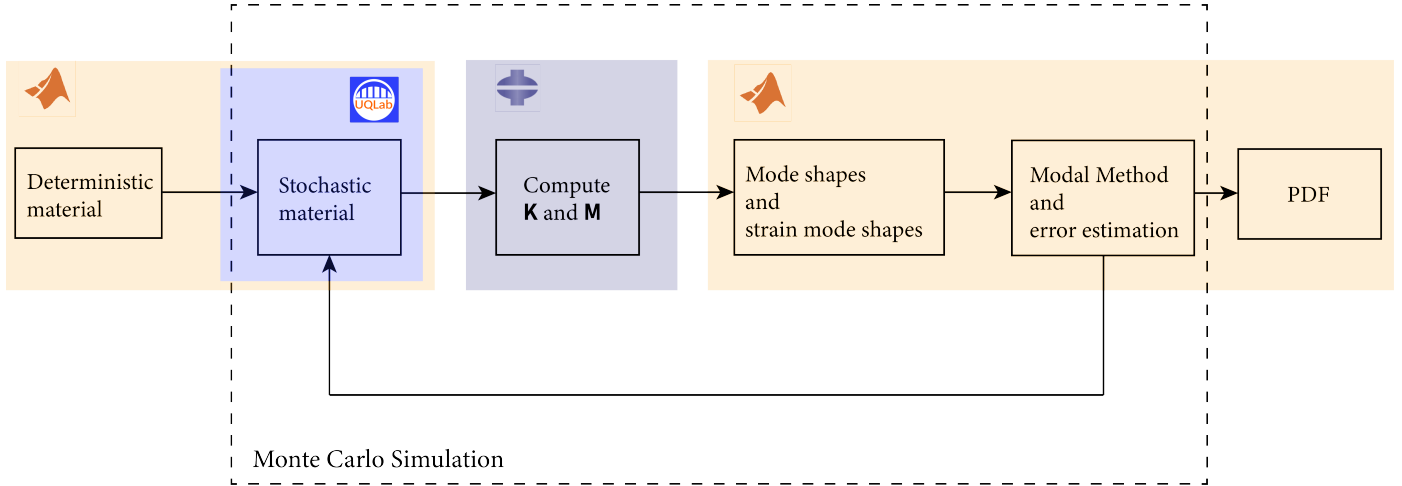
Figure 22: Workflow to assess how material uncertainty affects the results of MM.

		μ	σ	σ/μ	$(\mu - \text{exact})/\text{exact}$
CoV = 0.05	iFEM	0.073	0.01	0.137	−0.001
	MM	0.011	0.006	0.54	1.30
CoV = 0.1	iFEM	0.073	0.02	0.27	0
	MM	0.022	0.013	0.65	3

Table 4: *Comparison of the error distributions from Modal Method and iFEM for tip load case under measurement uncertainty.*

are presented, since the authors found similar observations for the other load cases. As it is possible to see from Table 4, the iFEM results show a lower CoV of the resulting distribution w.r.t. the Modal Method. Furthermore, the mean value μ almost coincides with the value unaffected by errors (exact). On the other hand, the Modal Method is relatively more affected by the input errors, but it is still able to deliver the best results in terms of the mean value of the distribution.

7.2. Material Uncertainty

Since iFEM is only based on strain-displacement relations and not on constitutive relations, the results are unaffected by uncertainties coming from the material properties. However, in the Modal Method the vibration modes need to be calculated, thus requiring the structural matrices that are affected by uncertainties in material properties. The following study investigates the effect of material uncertainties on the shape sensing reconstruction using the Modal Method, and compares the stochastic estimation error to iFEM. The material parameters considered are listed in Table 5, being each characterized by a normal distribution with the mean value being the reference value, and the standard deviation being respectively 5-10%μ. In Table 5, t is the ply thickness, ρ the material density, and θ the ply angle. Note that for the ply angle θ, the standard deviations are $\sigma = \{2°, 4°\}$. Furthermore, the iteration index $k = \{1, 2\}$ is used to indicate that two increasing uncertainty levels are evaluated. The stochastic materials which are created within the Monte Carlo scheme are then used as an input for MM. The workflow

is briefly summarized in Figure 22. First, the stochastic material is created starting from the reference values of the deterministic one. Then, the mass M and stiffness K matrices are computed based on this input, using `Abaqus` as an external finite element package. Next, the mode shapes can be obtained from which the corresponding strain mode shapes are computed. With matrices Φ and Ψ of Eq.(5) being computed, the final displacement can be retrieved. This procedure is repeated in order to estimate the final PDF of the shape sensing error. A number of 500 iterations has been carried out since it was observed a converged distribution with this sample size.

	μ	σ
$E_1, E_2, \nu_{12}, G_{12}, G_{13}, G_{23}, \rho, t$	nominal	$(0.05\mu)\,k$
θ (ply angle)	nominal	$2°\,k$

Table 5: *Stochastic material parameters.*

Reporting only the results of the tip load case, the PDF of Figure 23 is obtained where also the error from iFEM (unaffected by the material uncertainty) is shown. In general, the mean of the error distribution shifts to higher values increasing the variance of the input random variables but, for the cases studied, it remains lower compared to the failure predicted by iFEM. The PDF plot however does not provide any information about how the mode shapes are altered by the random material properties. In this study, only the natural frequencies distribution of the corresponding mode shapes has been studied and it is reported in Figure 24. Their values tend to quickly spread over a large interval, especially for the higher modes. This points to the fact that, even if the natural frequencies are not exactly matched, shape sensing employing MM can still yield relatively good results.

8. Conclusions

This study presented the successful development of an improved Inverse Finite Element Method (iFEM) applicable for
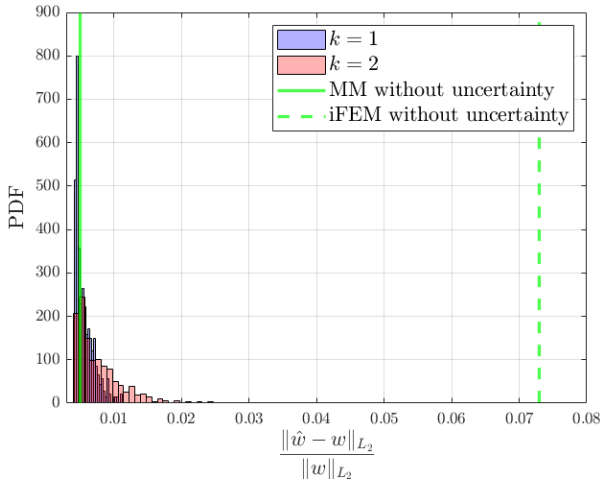
Figure 23: *Probability density function of relative L2-norm error of vertical displacement estimated with Monte Carlo Simulation for Modal Method for tip load case under material uncertainty.*
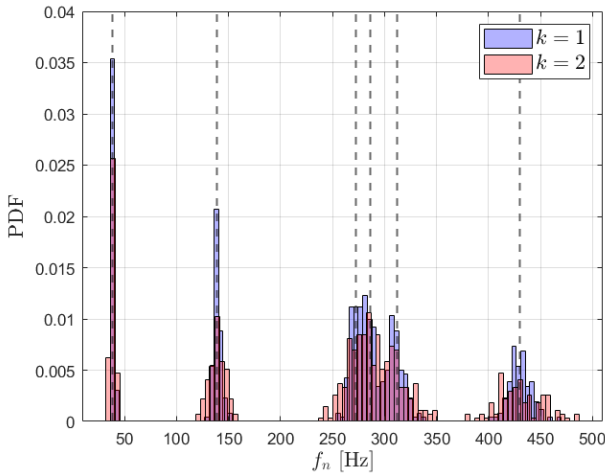

Figure 24: *Distribution of natural frequencies under material uncertainty.*

wing-like structures when only sparse strain measurements are available.

The proposed improvement was enabled from a preliminary strain pre-extrapolation using Smoothing Element Analysis (SEA). The available SEA three-node element from literature showed to be limited in modeling three-dimensional geometries due to the required arbitrary choice of some scalar parameters, that is the scalar coefficient α in the minimization of the SEA functional and the drilling stiffness k_{ψ_z}. To overcome this limitation, a four-node element was developed, which led to better a better outcome: the results showed to be far less dependent on k_{ψ_z} and the parameter α can be chosen with a simple method plotting the residuals Φ_ε and Φ_α in a log-log plot.

The study also compared the improved iFEM with the Modal

Method. An uncertainty quantification analysis exhibits how the reconstruction is affected by errors in the strain measurements and material properties. In general, the Modal Method is more sensitive to measurements errors when compared to iFEM, and is the only method affected by errors present in the material properties. Nevertheless, even taking into account the larger sensitivity of the Modal Method towards measurement uncertainties, for the cases investigated it recovers the lowest means of the error distributions. A large limitation of the applicability of the Modal Method comes from the fact that the structural modes must be known in advance, either via experimental modal analysis or numerically with the calculation of the structural mass and stiffness matrices. In cases where the structural matrices cannot be obtained in a reliable manner, the improved iFEM herein developed remains as the only available option.

Future studies should analyze the displacement reconstruction for a more general sensor configuration. As outlined in the paper, only discrete strain rosettes have been considered here and therefore the strain field can be rotated in the inverse element reference system without incurring into additional problems. If only axial strain measurements are available, the strain rotation operation would mix actual strain measurements with pre-extrapolated ones, which for instance could have been obtained with SEA.

References

[1] A. Tessler, J. Spangler, Inverse FEM for Full-Field Reconstruction of Elastic Deformations in Shear Deformable Plates and Shells, Proceedings of Second European Workshop on Structural Health Monitoring (2004) 83–90.

[2] P. Bogert, E. Haugse, R. Gehrki, Structural shape identification from experimental strains using a modal transformation technique, Collection of Technical Papers - AIAA/ASME/ASCE/AHS/ASC Structures, Structural Dynamics and Materials Conference 3 (April) (2003) 2026–2043. doi:10.2514/6.2003-1626.

[3] M. Esposito, M. Gherlone, Composite wing box deformed-shape reconstruction based on measured strains: Optimization and comparison of existing approaches, Aerospace Science and Technology 99 (2020). doi:10.1016/j.ast.2020.105758.

[4] D. Oboe, L. Colombo, C. Sbarufatti, M. Giglio, Comparison of strain pre-extrapolation techniques for shape and strain sensing by iFEM of a composite plate subjected to compression buckling, Composite Structures 262 (November) (2021). doi:10.1016/j.compstruct.2021.113587.

[5] A. Tessler, H. Riggs, S. Macy, A variational method for finite element stress recovery and error estimation, Computer Methods in Applied Mechanics and Engineering 111 (3-4) (1994) 369–382. doi:10.1016/0045-7825(94)90140-6.

[6] A. Tessler, H. Riggs, C. Freese, G. Cook, An improved variational method for finite element stress recovery and a posteriori error estimation, Computer Methods in Applied Mechanics and Engineering 155 (1-2) (1998) 15–30. doi:10.1016/S0045-7825(97)00135-7.

[7] P. Minigher, J. Gundlach, S. G. P. Castro, ISTAR Demo Wing Abaqus Model [Data set], Zenodo. https://doi.org/10.5281/zenodo.7030874 (2022).

[8] J. Dillinger, T. Klimmek, J. Gundlach, Finite Element Model of the IS-TAR Demonstrator Wing [Data set], Zenodo. https://doi.org/10.5281/zenodo.7017137 (2022).

[9] S. Rapp, L. Kang, J. Han, U. Mueller, H. Baier, Displacement field estimation for a two-dimensional structure using fiber Bragg grating sen-

sors, Smart Materials and Structures 18 (2) (feb 2009). `doi:10.1088/0964-1726/18/2/025006`.

[10] L. Li, W. Li, P. Ding, X. Zhu, W. Sun, Structural shape reconstruction through modal approach using strain gages, Communications in Computer and Information Science 462 (2014) 273–281.

[11] H. Bang, S. Ko, M. Jang, H. Kim, Shape estimation and health monitoring of wind turbine tower using a FBG sensor array, 2012 IEEE I2MTC - International Instrumentation and Measurement Technology Conference, Proceedings (3) (2012) 496–500. `doi:10.1109/I2MTC.2012.6229407`.

[12] A. Kefal, E. Oterkus, A. Tessler, J. Spangler, A quadrilateral inverse-shell element with drilling degrees of freedom for shape sensing and structural health monitoring, Engineering Science and Technology, an International Journal 19 (3) (2016) 1299–1313. `doi:10.1016/j.jestch.2016.03.006`.

[13] M. Esposito, M. Gherlone, Material and strain sensing uncertainties quantification for the shape sensing of a composite wing box, Mechanical Systems and Signal Processing 160 (2021). `doi:10.1016/j.ymssp.2021.107875`.

[14] M. Gherlone, P. Cerracchio, M. Mattone, Shape sensing methods: Review and experimental comparison on a wing-shaped plate, Progress in Aerospace Sciences 99 (September) (2018) 14–26. `doi:10.1016/j.paerosci.2018.04.001`.

[15] M. A. Abdollahzadeh, A. Kefal, M. Yildiz, A comparative and review study on shape and stress sensing of flat/curved shell geometries using c0-continuous family of iFEM elements, Sensors (Switzerland) 20 (14) (2020) 1–22. `doi:10.3390/s20143808`.

[16] A. Tessler, H. Riggs, M. Dambach, A novel four-node quadrilateral smoothing element for stress enhancement and error estimation, International Journal for Numerical Methods in Engineering 44 (10) (1999) 1527–1543. `doi:10.1002/(SICI)1097-0207(19990410)44:10<1527::AID-NME497>3.0.CO;2-1`.

[17] H. Riggs, A. Tessler, H. Chu, C1-continuous stress recovery in finite element analysis, Computer Methods in Applied Mechanics and Engineering 143 (3-4) (1997) 299–316. `doi:10.1016/S0045-7825(96)01151-6`.

[18] A. Tessler, J. Spangler, M. Mattone, M. Gherlone, M. Di Sciuva, Real-time characterization of aerospace structures using onboard strain measurement technologies and inverse finite element method, Structural Health Monitoring 2011: Condition-Based Maintenance and Intelligent Structures - Proceedings of the 8th International Workshop on Structural Health Monitoring 1 (2011) 981–988.

[19] C. L. Lawson, R. J. Hanson, Solving Least Squares Problems, Society for Industrial and Applied Mathematics, 1995.

[20] P. C. Hansen, D. P. O'Leary, The Use of the L-Curve in the Regularization of Discrete Ill-Posed Problems, SIAM Journal on Scientific Computing 14 (6) (1993) 1487–1503. `doi:10.1137/0914086`.

[21] S. Marelli, B. Sudret, UQLab: A Framework for Uncertainty Quantification in MATLAB, The 2nd International Conference on Vulnerability and Risk Analysis and Management (2014).